JBC RESEARCH ARTICLE

Distinct neurotoxic TDP-43 fibril polymorphs are generated by heterotypic interactions with α-Synuclein

Received for publication, June 29, 2022, and in revised form, September 8, 2022 Published, Papers in Press, September 16, 2022,
https://doi.org/10.1016/j.jbc.2022.102498

Shailendra Dhakal[1,2], Alicia S. Robang[3], Nemil Bhatt[4], Nicha Puangmalai[4], Leiana Fung[4], Rakez Kayed[4], Anant K. Paravastu[3,*], and Vijayaraghavan Rangachari[1,2,*]

From the [1]Department of Chemistry and Biochemistry, School of Mathematics and Natural Sciences; [2]Center for Molecular and Cellular Biosciences, University of Southern Mississippi, Hattiesburg, Mississippi, USA; [3]School of Chemical and Biomolecular Engineering, Georgia Institute of Technology, Atlanta, Georgia, USA; [4]Mitchell Center for Neurodegenerative Disorders, University of Texas Medical Branch, Galveston, Texas, USA

Edited by Ursula Jakob

Amyloid aggregates of specific proteins constitute important pathological hallmarks in many neurodegenerative diseases, defining neuronal degeneration and disease onset. Recently, increasing numbers of patients show comorbidities and overlaps between multiple neurodegenerative diseases, presenting distinct phenotypes. Such overlaps are often accompanied by colocalizations of more than one amyloid protein, prompting the question of whether direct interactions between different amyloid proteins could generate heterotypic amyloids. To answer this question, we investigated the effect of α-synuclein (αS) on the DNA-binding protein TDP-43 aggregation inspired by their coexistence in pathologies such as Lewy body dementia and limbic predominant age-related TDP-43 encephalopathy. We previously showed αS and prion-like C-terminal domain (PrLD) of TDP-43 synergistically interact to generate toxic heterotypic aggregates. Here, we extend these studies to investigate whether αS induces structurally and functionally distinct polymorphs of PrLD aggregates. Using αS–PrLD heterotypic aggregates generated in two different stoichiometric proportions, we show αS can affect PrLD fibril forms. PrLD fibrils show distinctive residue level signatures determined by solid state NMR, dye-binding capability, proteinase K (PK) stability, and thermal stability toward SDS denaturation. Furthermore, by gold nanoparticle labeling and transmission electron microscopy, we show the presence of both αS and PrLD proteins within the same fibrils, confirming the existence of heterotypic amyloid fibrils. We also observe αS and PrLD colocalize in the cytosol of neuroblastoma cells and show that the heterotypic PrLD fibrils selectively induce synaptic dysfunction in primary neurons. These findings establish the existence of heterotypic amyloid and provide a molecular basis for the observed overlap between synucleinopathies and TDP-43 proteinopathies.

Many neurodegenerative proteinopathies are characterized by the deposition of misfolded protein aggregates called amyloids in neuronal and glial cells (1–4). These disorders affect diverse neuroanatomical regions in the brain and exhibit clinical heterogeneity (5–7). Although each protein aggregation disease is often presumed to be caused by misfolding of a single protein, ostensibly distinct neurodegenerative pathologies can show significant clinical and pathological overlap (8–10). It appears the phenotype variations may be attributed in part to the interactions between two or more amyloid proteins and accumulation of biochemically distinct heterotypic protein aggregates. For example, aggregates of both tau and αS have been observed in numerous pathologies that are collectively known as tauopathies and synucleinopathies, respectively (11, 12). Indeed, preponderance of interactions between amyloid-β (Aβ), tau, α-synuclein (αS), and transactive response DNA-binding protein 43 kDa (TDP-43) suggests that heterotypic amyloid aggregates may be significant in pathology (13–19). A cornucopia of evidence indicates spatial localization and coexistence of more than one amyloidogenic protein in many proteinopathies. Although not a ubiquitous phenomenon, some amyloid proteins show a greater degree of colocalization than the others such as tau and αS. For example, tau aggregates are often observed in multiple neurodegenerative diseases such as Alzheimer dissease, Parkinson disease, multiple system atrophy, frontotemporal lobar degeneration (FTLD) etc. (20–22). Similarly, in addition to its presence in Lewy body diseases (LBDs), aggregates of αS are often observed in the aforementioned pathologies alongside tau deposits (23). Because of their widespread presence in numerous pathologies, the disorders with lesions enriched in tau and αS are termed as tauopathies and synucleinopathies, respectively (21, 24). Yet another protein whose insoluble amyloid inclusions are nearly as widespread as those with tau and αS is TDP-43, its presence is increasingly becoming known in at least 15 different neurodegenerative diseases including Alzheimer dissease, Parkinson disease, ALS, and FTLD and seems to be a key component in the rapidly expanding spectrum of TDP-43 proteinopathies (25). A subset of this spectrum shows overlap with LBDs in which αS aggregates predominate, suggesting colocalization and potential interactions between the TDP-43 and αS. Indeed, mounting evidence indicates synergism between the two protein deposits. In LBD, the severity of αS pathology in the temporal cortex was observed to be significantly more among TDP-43

* For correspondence: Vijayaraghavan Rangachari, vijay.rangachari@usm.edu; Anant K. Paravastu, anant.paravastu@chbe.gatech.edu.

positive patients, which correlated with the severity of TDP-43 pathology in the amygdala (26). Perhaps the most compelling evidence for selective influence of αS on TDP-43 proteinopathy comes from LATE patient brains in which distinct neuropathological changes are observed in PrLD/αS aggregates containing LATE-LBD and LATE-AD copathologies compared to pure LATE (27).

The involvement of TDP-43 in diverse pathophysiological functions has refocused attention to its role in a wide range of neurodegenerative pathologies involving αS aggregates. TDP-43 is a 43 kDa protein that belongs to the ribonucleoprotein family. TDP-43 consists of an N-terminal domain, two RNA-recognition motifs, RRM1 and RRM2, and a disordered, prion-like C-terminal domain (PrLD) (28, 29). Under physiological conditions, the protein is localized predominantly in the nucleus and plays a role in transcriptional regulation, RNA alternative splicing, miRNA biogenesis, transport, and stabilization (29–31). In pathology, TDP-43 translocates to the cytoplasm, where it undergoes posttranslational modifications including phosphorylation, ubiquitination, and aberrant proteolytic cleavage to generate multiple C-terminal fragments (32–35). These fragments, ranging from approximately 17 kDa (corresponding to PrLD) to 35 kDa, form insoluble cytoplasmic aggregates and toxic inclusions in cells (33, 36–38). αS is a 14.6 kDa, intrinsically disordered protein containing three domains: amphipathic N-terminal domain, central aggregation-prone nonamyloid component, and an intrinsically disordered charged C-terminal domain (39, 40). As noted, although αS and TDP-43 are known to form cytoplasmic amyloid inclusions independently, the question of whether aggregation of the two proteins can be synergistic and coupled to one another has not been addressed in detail. This question is pertinent given the fact that the two proteins are known to influence each other. For example, coexpression of αS and TDP-43 enhances neurodegeneration and loss of dopaminergic neurons in *Caenorhabditis elegans* and transgenic mice (41, 42). Similarly, incubation of exogenous αS fibrils in SH-SY5Y cells enhances TDP-43 phosphorylation and aggregation (43). More compelling pathological evidence of the interaction between the two proteins comes from a recent study that showed that TDP-43 aggregates coexist with αS aggregates in LATE-LBD and LATE-AD copathologies, exhibiting histopathological differences between pure LATE, LATE-LBD, and LATE-AD (27). These observations also suggest that the polymorphic fibrils of TDP-43 observed in these patients could be consequential of the influence by αS. Structural polymorphism is known to exist among many amyloid proteins; however, only a few polymorphic strains of TDP-43 fibrils derived from patients have come to the limelight so far (44–48). More importantly, the correlation between structure, biophysical properties, and pathophysiology of TDP-43 polymorphs remains unclear. Thus, we ask the question whether polymorphic strains of one amyloid protein can be induced by another amyloidogenic protein. Despite evidence for cross-interactions between amyloid proteins such as those for amyloid-β (Aβ) and islet amyloid polypeptide (IAPP), αS and Aβ, αS and Tau (13, 18, 49–51), the answer to this question remains elusive especially for αS and TDP-43.

Recently, to uncover the mechanistic understanding between the two proteins, we showed that equimolar amounts of αS and PrLD monomers interact synergistically to form coaggregated, hybrid fibrils (52). In the same report, we also showed that oligomers and fibrils of αS cross-seed PrLD fibril formation selectively but preformed PrLD fibril fails to seed αS monomers hinting at possible conformational selection in cross-interactions between the two proteins. In this report, we extend these investigations to answer the important question of whether cross-seeding of αS to TDP-43 or heterotypic coaggregation of the two proteins induce specific polymorphic fibrils of TDP-43 compared to the unseeded TDP-43. We show that PrLD aggregation is sensitive to the αS aggregate characteristics; both PrLD–αS hybrid fibrils generated by the interactions of the two monomers and αS fibril (αS^f)-seeded PrLD fibrils show distinctive differences in structural and biophysical characteristics from PrLD homotypic fibrils formed in the absence of αS. We also show that the two proteins colocalize in the cytoplasm of the SH-SY5Y neuroblastoma cells and that PrLD heterotypic aggregates selectively induce synaptic dysfunction in primary neurons. These results help us understand the generation and propagation of heterotypic αS-TDP-43 amyloid polymorphs and their significance in many neurodegenerative maladies.

Results

PrLD and αS colocalize as puncta in the cytoplasm of SH-SY5Y neuroblastoma cells

While co-occurrence of TDP-43 encephalopathy and LBDs has been reported in the previous studies (13, 27) and our recent study showed synergistic interactions between PrLD and αS (52), it is unclear whether the two proteins colocalize in the cytoplasm. To investigate this, confluent SH-SY5Y neuroblastoma cells were separately transfected with the plasmids of blue fluorescent protein (sBFP2)-tagged PrLD and sBFP2 alone as a control. After 24 h of incubation at 37 °C to allow transient expression, both the PrLD-expressing and control cells were pulsed with Hilyte-532-labeled 500 nM recombinant αS monomers prepared in 20 mM MES buffer (detailed in Experimental procedures) and incubated for additional 24 h to ensure the maximum internalization as reported previously (53). Live-cell imaging after adding nuclear stain under a confocal microscope revealed that the control sBFP2-expressing cells exhibited diffused blue fluorescence throughout the cells with a few denser foci in the cytoplasm. At the same time, the internalized αS monomers were present in the diffused form in the cytoplasm as anticipated (Fig. 1*A*). Thus, sBFP2 and αS did not show colocalization but remained primarily diffused. In contrast, sBFP2-PrLD expressing cells showed distinct fluorescent puncta present exclusively in the cytoplasm, which we believe are PrLD aggregates (Fig. 1*B*). Interestingly, internalized αS (*yellow*) showed colocalization within the puncta of PrLD (Fig. 1*B*). Based on our previous finding that showed synergistic coaggregation between αS and PrLD monomers and selective seeding of PrLD monomers by αS aggregates (52), we conjecture that the colocalized puncta

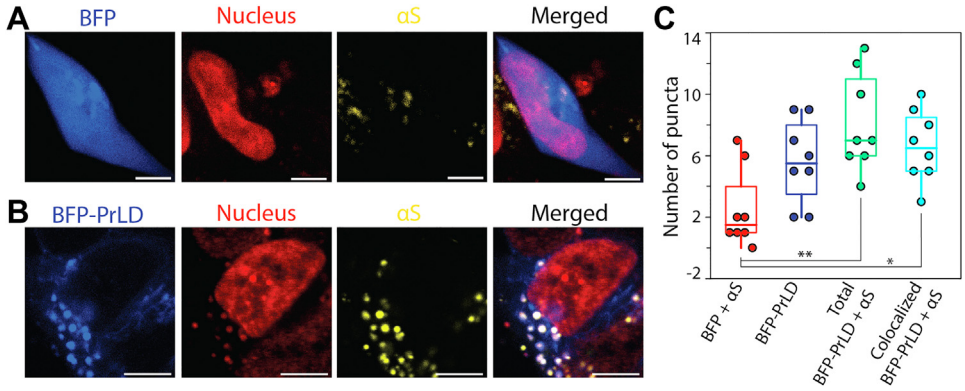

Figure 1. Representative live-cell images showing colocalization of αS with blue fluorescent protein (BFP) and BFP-tagged prion-like domain (BFP-PrLD). Fluorescent confocal images of human SH-SY5Y neuroblastoma cells 48 h after transfection with BFP (*A*) and BFP-PrLD (*B*). Cells were pulse-chased with Hilyte-532 fluorescently labeled monomeric recombinant αS (*yellow*) 24 h post-transfection. Cells were stained with nuclear stain (*red*) prior to confocal live-cell imaging at 40× magnification. Merged panel shows degree of cytoplasmic colocalization of αS with BFP and BFP-PrLD (Scale bar = 5 μm). *C*, box plot showing number of cytoplasmic puncta observed in cells transiently expressed with BFP or BFP-PrLD, with or without coincubated αS (n= 8 independent cells); **p* <0.05, ***p* <0.005.

are predominantly heterotypic aggregates of αS and PrLD monomers or oligomers. This conjecture is supported by the presence of PrLD puncta devoid of αS alongside colocalized puncta containing both PrLD and αS (Fig. 1*C*). Moreover, no significant difference was observed between the colocalized puncta and the total number of puncta (colocalized and isolated) (Fig. 1*C*; *green* and *blue*). These suggest that isolated PrLD puncta are formed prior to introducing αS, which can be oligomers, protofibrils, or fibrils. Lack of fluorescence recovery after photobleaching recovery on these puncta (54) indicated they are not droplets. The αS monomers taken up by the cells can potentially interact with monomers, as well as the aggregates of PrLD in the preformed puncta. Nevertheless, confirming cytoplasmic colocalization of the two proteins provides a cellular basis and support for their direct interactions (52) and potential formation of pathological polymorphs.

Gold nanoparticle-decorated transmission electron microscopy images support the existence of heterotypic hybrid fibrils of αS and PrLD

First, morphological features of heterotypic aggregates were investigated by negative staining transmission electron microscopy (TEM). Both homotypic PrLD and αS fibrils showed smooth and long unbranched fibrils, as expected (Fig. 2, *A* and *B*). In contrast, both PrLD–αS hybrid and $αS^f$-seeded PrLD fibrils showed more branching and clumping in their fibrillar structures (Fig. 2, *C* and *D*). To quantify the amounts of αS and PrLD within the fibrils, samples were treated with formic acid (to disaggregate the fibrils) and subjected to MALDI-TOF analysis. The homotypic PrLD showed the expected mass (Fig. 2*E*). The PrLD–αS hybrid fibrils showed the presence of approximately equimolar amounts of αS and PrLD as shown in our previous study (52) (Fig. 2*F*). Since αS fibrils were added as substoichiometric seed, as expected, αS was barely detectable in the $αS^f$-seeded PrLD fibrils (Fig. 2*G*). All the samples also showed low amounts of sinapinic acid adducts, which has been shown to be common with this matrix (55). To establish the formation of heterotypic aggregates, PrLD–αS hybrid fibrils were investigated using Au-nanoparticle–labeled TEM. Substoichiometric hexa-histidine tagged protein to facilitate nanogold particle binding was mixed with the untagged protein (hetero or homo) and incubated for fibril formation (see Experimental procedures). Fibrils were then isolated and incubated with Au-nanoparticles to be visualized by TEM (Fig. 2*H*). The positive control, homotypic PrLD fibrils, were prepared by mixing 5 μM his-tagged PrLD with 20 μM untagged PrLD fibrillar structures studded with Au-nanoparticles (Fig. 2*I*). Images of Au-nanoparticle incubated PrLD–αS hybrid fibrils containing his-tagged αS and untagged PrLD also showed the presence of Au-nanoparticle studded fibrils confirming the presence of both PrLD and αS within the sample fibrils. In other words, there is a hybrid heterotypic PrLD–αS polymorph (Fig. 2*J*).

αS-induced PrLD fibril polymorphs exhibit biophysical differences

To further examine the conformational differences among PrLD polymorphs generated by the interactions with αS, intrinsic tryptophan fluorescence along with binding to known amyloid dyes such as 8-anilinonaphthalene-1-sulfonic acid (ANS), curcumin, and 9-(dicyano-vinyl) julolidine (DCVJ) were measured. First, homotypic PrLD fibrils generated in the absence of αS, hybrid fibrils generated by incubating equimolar amount of PrLD, and αS monomers and $αS^f$-seeded PrLD fibrils along with controls were analyzed for intrinsic tryptophan fluorescence. Fibrils were prepared as reported in our previous study (52), (detailed in Experimental procedures). All three samples, PrLD–αS hybrid fibrils, $αS^f$-seeded PrLD fibrils, and homotypic PrLD control fibrils showed blue shifts compared to PrLD monomers ($λ^{Em}$ = 340 nm), reflecting a solvent-protected apolar environment within the fibrils (Fig. 3*A*). Among the samples, hybrid fibrils showed marginally greater blue shift (Δλ = |12| nm) as compared to $αS^f$-seeded PrLD (Δλ = |9| nm) or control PrLD fibrils (Δλ = |8| nm). However, the intensities for both control PrLD and PrLD–αS hybrid fibrils showed a significant decrease while $αS^f$-seeded PrLD

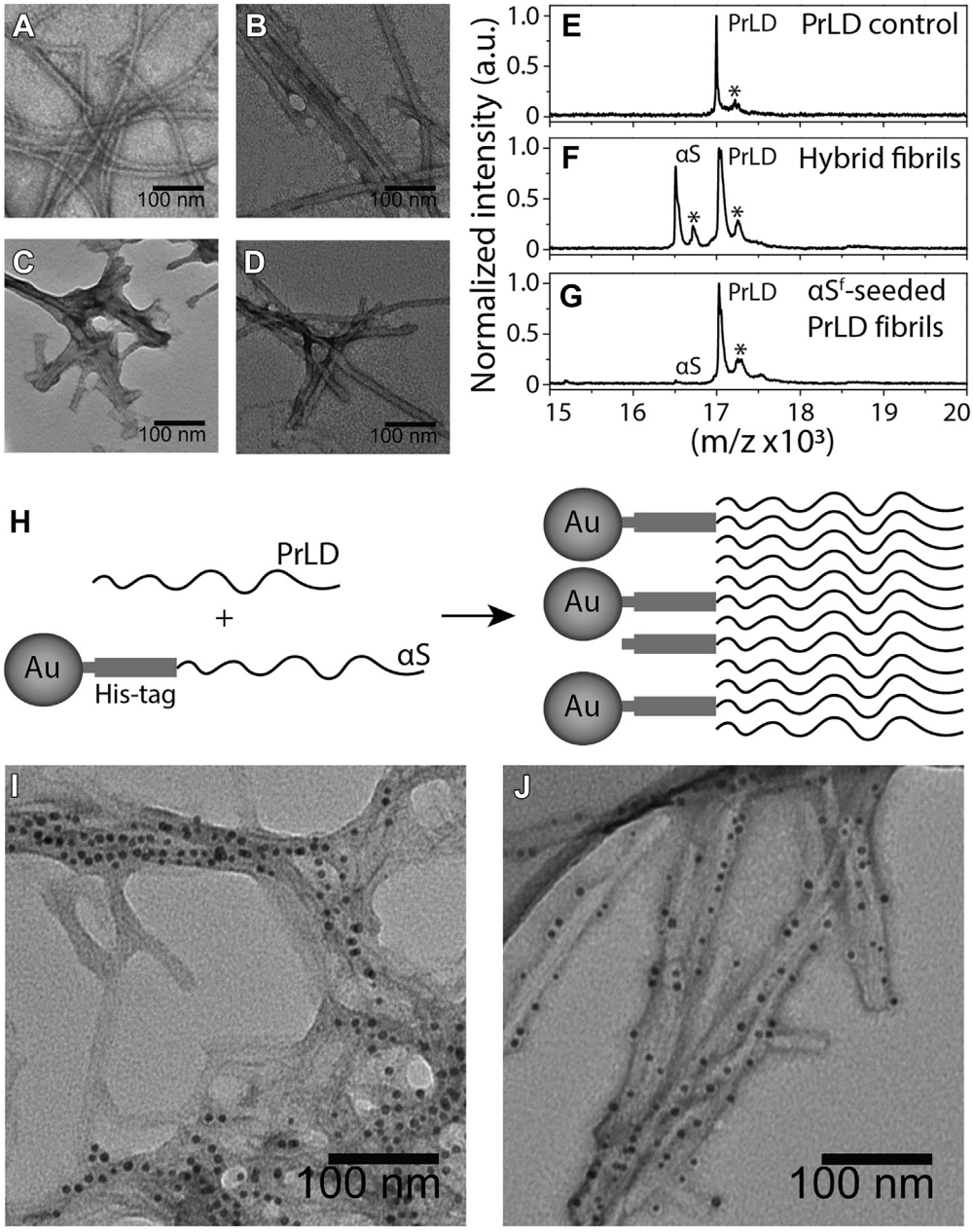

Figure 2. TEM images of unlabeled and nanogold-labeled fibrils along with their MALDI-TOF spectra *A–E*, negative EM staining of (*A*) homotypic PrLD fibrils, (*B*) homotypic αS fibrils, (*C*) hybrid fibrils, and (*D*) $αS^f$-seeded PrLD fibrils. *E–G*, normalized MALDI-ToF spectra of formic acid treated PrLD homotypic fibrils (*E*), hybrid fibrils (*F*), and $αS^f$-seeded PrLD fibrils (*G*) showing relative amount of αS and PrLD monomers. The '*' indicates the protein adduct formed with sinapinic acid (SA). *H*, schematic showing possible arrangement of Au-nanoparticle bound his-tagged αS with untagged PrLD in the hybrid fibrils. *I* and *J*, Ni-NTA Au-nanoparticle–labeled PrLD fibrils (*I*) and hybrid fibrils (*J*). *Black* dots on the fibrils are 5-micron nanogold particles bound to the hexa-histidine tag on αS or PrLD surface. TEM, transmission electron microscopy.

fibrils showed a small increase in intensity reflecting a more solvent-protected environment for latter (Fig. 3, *A* and *E*). Intrinsic fluorescence for control αS fibrils could not be monitored as the protein is devoid of tryptophan residues. The ANS dye, known to binding exposed hydrophobic surfaces (56, 57), also showed significant differences in both wavelength shifts and intensities (Fig. 3, *B* and *E*).

Surprisingly, PrLD–αS hybrid fibrils and $αS^f$-seeded PrLD fibrils showed no wavelength shift compared to monomers but both control PrLD and αS fibrils showed red shifts in the order of ($\Delta\lambda$ = |4.5| nm) and ($\Delta\lambda$ = 11| nm), respectively (Fig. 3, *B* and *E*). The intensity of ANS fluorescence, which reflects the extent of exposed hydrophobic surfaces, showed noticeable changes; here too, $αS^f$-seeded PrLD fibrils showed the largest percentage increase, followed by PrLD–αS hybrid fibrils and the control PrLD fibrils, while the control $αS^f$ showed a decrease in the intensity (Fig. 3, *B* and *E*). Curcumin, which is known to bind and distinguish different aggregate structures (58, 59), also showed significant blue shifts in wavelength that were somewhat uniform in magnitude ($\Delta\lambda$ = ∼|15| nm) except for control αS fibrils ($\Delta\lambda$ = ∼|8| nm) (Fig. 3, *C* and *E*). The intensities for the same samples, however, showed variations;

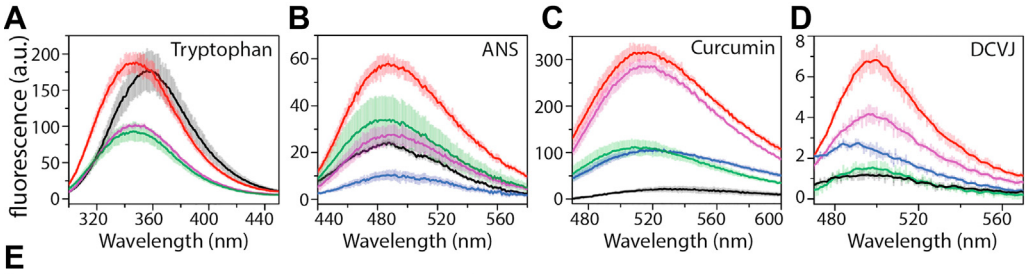

E

Dye		αS fibrils	TDP-43 PrLD fibrils	Hybrid fibrils	αS^f-seeded TDP-43 PrLD
Tryptophan	$\Delta\lambda_{Em}^{max}$ (nm)	-	-8.50 ± 1.04	-11.67 ± 2.00	-9.34 ± 0.76
	% Int. change	-	-42.14	-46.25	8.42
ANS	$\Delta\lambda_{Em}^{max}$ (nm)	11.72 ± 3.24	4.57 ± 0.55	-0.04 ± 0.76	0.33 ± 0.57
	% Int. change	-56.32	21.75	50.28	157.69
Curcumin	$\Delta\lambda_{Em}^{max}$ (nm)	-8.16 ± 1.61	-15.33 ± 1.99	-15.66 ± 3.88	-14.17 ± 1.74
	% Int. change	448.03	1234.91	425.56	1420.23
DCVJ	$\Delta\lambda_{Em}^{max}$ (nm)	-0.32 ± 0.76	3.99 ± 0.06	2.33 ± 1.52	7.16 ± 0.76
	% Int. change	99.14	213.82	4.89	396.08

Figure 3. Intrinsic fluorescence and dye binding of heterotypic αS-TDP-43 PrLD species. *A–D*, intrinsic tryptophan, ANS, curcumin, and DCVJ fluorescence emission scans, respectively for TDP-43 PrLD monomers (—), αS fibrils (—), TDP-43 PrLD fibrils (—), αS-TDP-43 PrLD hybrid fibrils (—), and αS^f-seeded TDP-43 PrLD fibrils (—); n = 3 independent scans. *E*, table showing mean shift in tryptophan, ANS, curcumin, and DCVJ emission maxima ($\triangle\lambda_{Em}^{max}$) along with percentage change in total intensity (% Int. change) of αS fibrils, TDP-43 PrLD fibrils, αS-TDP-43 PrLD hybrid fibrils, and αS^f-seeded TDP-43 PrLD fibrils to TDP-43 PrLD monomers. Both monomers and fibrils (2 μM) were prepared in 20 mM MES buffer pH 6.0. Samples concentration was determined using Pierce BCA protein assay kit; fibrils concentration is expressed as monomer equivalents (see details in Experimental procedures). ANS, 8-anilinonaphthalene-1-sulfonic acid; BCA, bicinchoninic acid; DCVJ, 9-(dicyano-vinyl) julolidine.

again, αS^f-seeded PrLD fibrils showed the largest percentage increase (1420%), followed by control PrLD fibrils (1234%), while PrLD–αS hybrid fibrils and control αS fibrils showed lesser change (448%) (Fig. 3, *C* and *E*). Finally, the addition of the dye DCVJ showed dramatic red shifts in wavelength for αS^f-seeded PrLD fibrils (Δλ = |7| nm) followed by control PrLD (Δλ = |4| nm) and PrLD–αS hybrid (Δλ = |2.3| nm), while the control αS fibril showed negligible shift (Fig. 3, *D* and *E*). The αS^f-seeded PrLD fibril sample also showed a dramatic percentage increase (390%) and PrLD–αS hybrid fibrils showed no change in the intensity, and control PrLD and αS fibrils showed 200% and 100% increases, respectively (Fig. 3, *D* and *E*). Together, these data bring out the subtle yet important differences in the ability of the amyloid binding dyes to distinguish between fibril polymorphs of PrLD induced by αS. More importantly, each of the dyes were able to differentiate between PrLD–αS hybrid, αS^f-seeded, and control PrLD fibrils, bringing out the potential conformational differences between these three polymorphs.

To investigate the potential differences between PrLD–αS hybrid, αS^f-seeded PrLD, and control PrLD fibril polymorphs, their enzymatic stabilities were analyzed. First, to see how stable the polymorphs are toward enzymatic degradation, a broad-spectrum serine protease-proteinase K (PK) that is widely used to assess the stability and conformational differences of many amyloid proteins was used (60–62). The three fibril samples along with control αS fibrils were incubated with PK, and aliquots of the samples were quenched at various time points to investigate the kinetic stability of the fibrils for degradation. The samples were then analyzed using SDS-PAGE and MALDI-TOF mass spectrometry. PK digestion of control αS^f showed a predominant band at ∼28 kDa (Fig. 4*A*) but without other low molecular weight bands, presumably due to extensive digestion. Control PrLD fibrils showed bands near ∼10, 17, and 30 kDa along with a faint band smear, presumably due to the dissociation of higher molecular weight oligomers and fibrils (Fig. 4*A*). In addition to the predominant bands near 28 and 10 kDa, PrLD–αS hybrid fibrils and αS^f-seeded PrLD fibrils showed multiple digested bands near 50, 28 to 10, and 6 kDa that are different from those observed for the control fibrils (arrows; Fig. 4*A*). The bands corresponding to molecular weight larger than the individual proteins are likely dissociated oligomers of the fibrils. The temporal stability of the polymorphic fibrils also showed differences in the rate of digestion.

While the control fibrils showed barely any change in the intensity of the digested bands, the bands near 8, 10, and 50 kDa for the PrLD–αS hybrid and αS^f-seeded fibrils showed progressive disappearance with time, suggesting lesser enzymatic stabilities for the two fibrils (Fig. 4*A*). These data also indicate that heterotypic fibril structures have more accessibility for PK to cleave the polypeptide backbone in core-

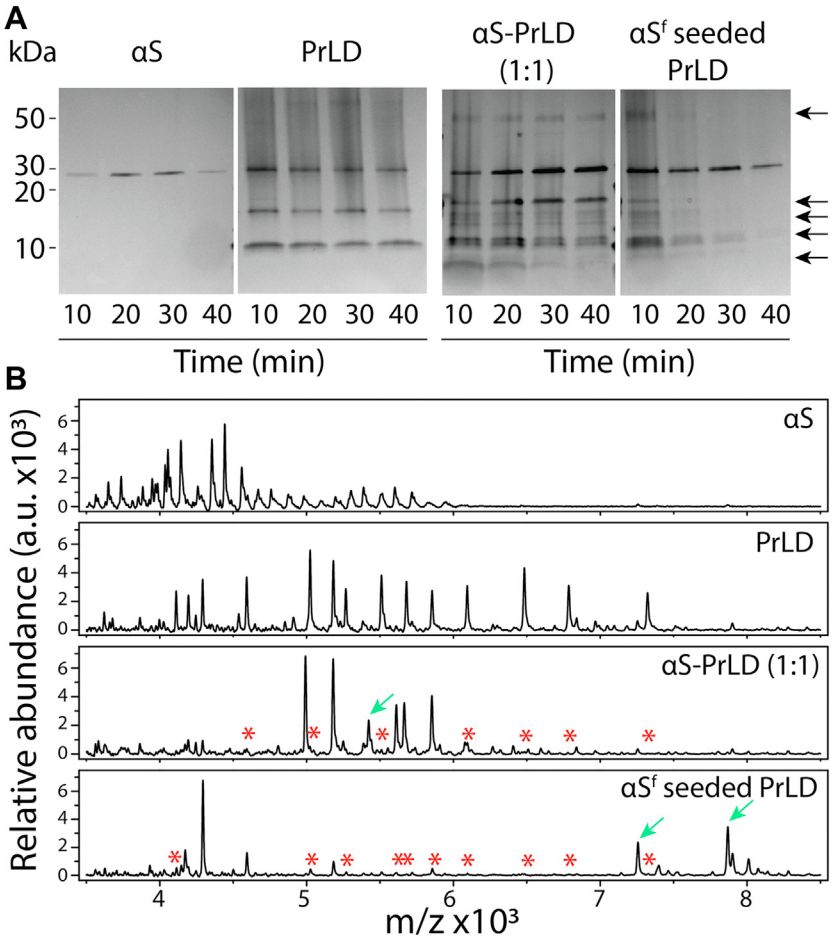

Figure 4. SDS-PAGE gel and MALDI-TOF spectra of proteinase K digested polymorphic αS and PrLD fibrils. *A*, proteinase K digestion of αS homotypic fibrils, PrLD homotypic fibrils, αS-PrLD (1:1) hybrid fibrils, and $αS^f$-seeded PrLD fibrils at different time points (10, 20, 30, and 40 min). *Arrows* indicate the digested bands unique to heterotypic fibrils. *B*, MALDI-TOF of proteinase K digested fragments from the same sample. *Arrows* (→) indicate the fragments unique to heterotypic fibrils, and star (*) indicate fragments that are absent in heterotypic ones.

amyloid regions or in other words, more amorphous than homotypic fibrils. To investigate the digestion pattern in the low molecular weight range (<8 kDa) that is not visible in SDS-PAGE gels, the same samples were analyzed by MALDI-TOF spectrometry. Homotypic control αS fibrils showed extensive digestion with numerous small molecular fragments (<6 kDa), which also answers why higher molecular weight fragmentations were not observed in the gel (Fig. 4*B*). The control PrLD fibrils also showed many fragments between 5 and 7 kDa (Fig. 4*B*). In contrast, the heterotypic fibril polymorphs showed fewer digested fragments but, more importantly, showed the absence of the digested fragments observed in the control along with some newer fragments suggesting a different structure for all the polymorphs (Fig. 4*B*).

Based on the PK digestion patterns, one could argue that the heterotypic fibril polymorphs of PrLD–αS hybrid, $αS^f$-seeded fibrils are more exposed to PK than the control homotypic PrLD fibrils. Therefore, it can be conjectured that the heterotypic polymorphs may show lesser thermodynamic stabilities than the homotypic PrLD fibrils. To test this interpretation, all samples were subjected to SDS treatment and denaturation and disaggregation as function of temperature. As established previously in our lab, SDS pretreatment can help reveal relative stabilities of amyloid aggregates since direct temperature increase does not "melt" amyloid aggregates (59). Typically, the conversion of β-sheets (fibrils) to α-helical structures (SDS-denatured and disaggregated) is monitored by far-UV CD as a function of temperature, and the degree of melting is represented as the ellipticity difference between 208 nm (α-helix) and 218 nm (β-sheet); more positive the difference is, more β-sheet the structure is.

The control homotypic PrLD fibrils, prior to SDS treatment and temperature increase, displayed an intense β-sheet spectrum with a minimum at 218 nm (premelt; Fig. 5*A*). An increase in temperature resulted in a conformational change to an α-helical structure with a midpoint of transition at ∼60 °C, typical for an amyloid fiber (Fig. 5, *A* and *E*). The fibrils also failed to convert to a complete α-helix even after 90 °C, suggesting high thermal stability (Fig. 5*E*). Heterotypic PrLD–αS hybrid fibrils showed a much less intense spectrum with a broad minimum at 214 to 218 nm, suggesting a less well-defined β-sheet signature prior to melting (premelt; Fig. 5*B*). Treatment of SDS immediately converted the spectrum to a partial α-helical structure, which became more defined and more intense with the increase in temperature (Fig. 5, *B* and *E*). Caution must be exercised with the intensity of the spectra as

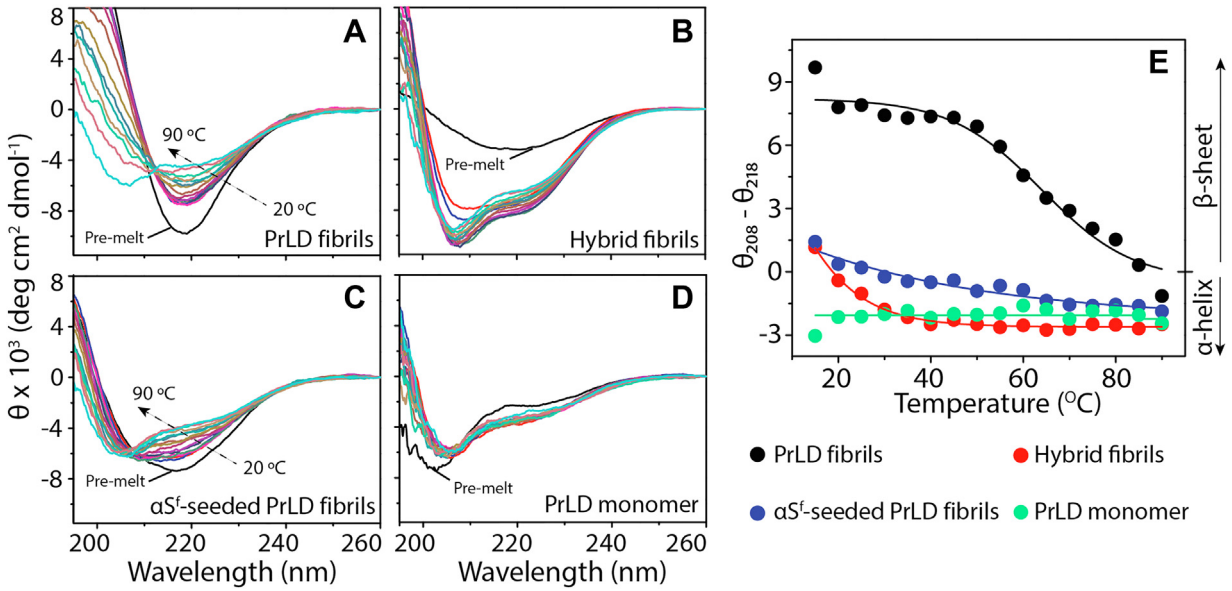

Figure 5. Differences in the thermal stabilities of αS-induced PrLD polymorphs suggest differences in their core structures. *A–D*, mean residue ellipticity [θ] from CD spectra obtained for homotypic PrLD fibrils (*A*), PrLD–αS hybrid fibrils (*B*), $αS^f$-seeded PrLD fibrils (*C*), and PrLD monomers (*D*) after treatment with 1% SDS and temperature increase from 20 °C to 90 °C. *E*, the difference in [θ] between 208 nm (α-helix) and 218 nm (β-sheet) is plotted as a function of temperature and fitted with Boltzmann's sigmoidal fits.

the data were normalized based on our assumed 1:1 stoichiometry for PrLD: αS within the fibrils (Fig. 1*A*) (52). Nevertheless, nearly half of the β-sheet melted to helix at 20 °C and completely at 40 °C, which suggests that the fibrils are more amorphous and less stable than the homotypic PrLD ones (Fig. 5*E*). $αS^f$-seeded PrLD fibrils showed an intense minimum at 218 nm (β-sheet) with a shoulder near 210 nm before melt, indicating the presence of an α-helical component within the fibrils to some degree (premelt; Fig. 5*C*). This result suggests a structure that is different from the homotypic fibrils. Treatment with SDS at 20 °C showed nearly half of the structure converted to an α-helix similar to PrLD–αS hybrid fibrils (Fig. 5, *C* and *E*). But, subsequent melting upon increasing temperature showed a slow and gradual conversion to a complete helical structure at 90 °C (Fig. 5*E*). As expected, the control PrLD monomers showed a predominant random coil structure with a partial α-helix as it is known to have a helical segment in the middle (63) that almost immediately melted to a complete α-helix (Fig. 5, *D* and *E*). The date collectively indicates that both PrLD–αS hybrid and $αS^f$-seeded PrLD fibrils differ in their structures, sensitivity toward SDS denaturation, and thermal stability from homotypic PrLD fibrils. Both heterotypic fibrils seem to be more amorphous, SDS-unstable fibrils, which seems to correlate with the PK enzymatic stability.

PrLD amyloid molecular structure is sensitive to αS interactions

NMR spectra indicate that PrLD molecular structure differs between PrLD–αS hybrid, $αS^f$-seeded PrLD fibrils, and control PrLD control fibrils (Fig. 6). In these experiments, only PrLD was isotopically labeled with ^{13}C. The spectra directly report on PrLD structure influenced by the interactions with αS. The molecular structure of PrLD within the amyloid core depends on whether PrLD fibrils are homotypic, formed in the absence of αS (Fig. 6*A*), $αS^f$-seeded PrLD fibrils (Fig. 6*B*), or PrLD–αS hybrid fibrils (formed by equimolar coincubation of PrLD and αS monomers in solution) (Fig. 6*C*). The NMR techniques employed (crosspolarization as well as dipolar assisted rotational resonance dipolar recoupling (64, 65)) are expected to yield signals from rigid regions of the spectrum (66) and thus produce signals only from the amyloid core structure. Furthermore, for the 50 ms mixing time employed for ^{13}C-^{13}C dipolar couplings the off-diagonal peaks are mainly due to ^{13}C-^{13}C interactions between atoms within the same amino acids or adjacent amino acids in the primary structure. Noting that the primary structure of the PrLD or the NMR experimental parameters did not vary between samples, the appearance of NMR crosspeaks in some spectra and not others indicates sample-dependent differences in the amyloid core regions. It is expected that protein backbone motion in the presence of water (samples were hydrated ultracentrifuge pellets) would suppress crosspeaks for molecular domains outside of the amyloid core. Another factor that would reduce detectability of signals outside the amyloid core is inhomogeneous broadening, caused a greater distribution of molecular conformations expected for regions outside of the amyloid core. To further illustrate the differences between the samples, Fig. 6*D* shows overlaid ^{13}C spectra for the three fibril samples.

Although further research is necessary to determine the detailed effects of αS on TDP-43 aggregated structure, molecular structural variation is evident in Fig. 6. To guide the eye, we circled selected regions of the spectrum and further note that some residues occur sparsely in the PrLD sequence. The regions 1, 2, 6, 8, 9, and 10 in Fig. 6 indicate crosspeaks between ^{13}C atoms in residues that are low abundance or rarely occur in the PrLD sequence (including E, D, Y, W, I, and L) (67). These regions also include several crosspeaks that

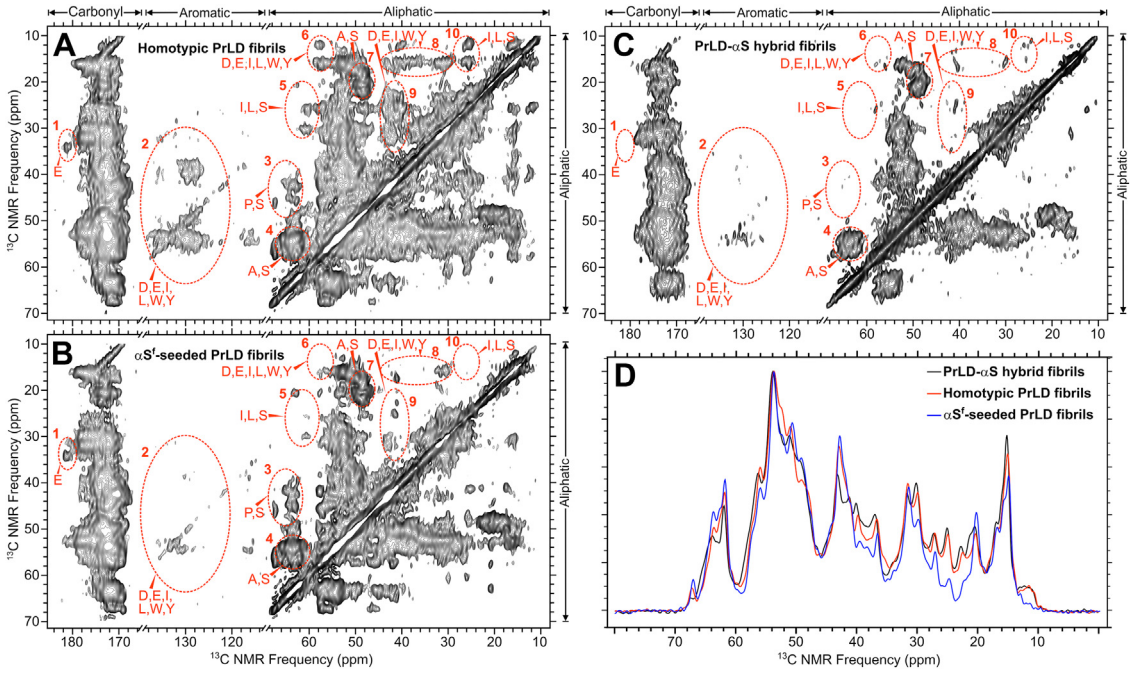

Figure 6. ^{13}C NMR spectra of uniformly ^{13}C-labeled TDP-43 PrLD in amyloid fibrils. Spectra correspond to: 2D ^{13}C-^{13}C unseeded homotypic PrLD fibrils (*A*), αS^{f}-seeded PrLD fibrils (*B*), and heterotypic PrLD–αS hybrid fibrils (*C*) and overlaid aliphatic regions (scaled for equal total intensity) of the ^{13}C NMR spectra from all three samples (*D*). The αS protein was not labeled with ^{13}C and therefore did not contribute directly to the spectra and the amino acids likely to contribute signal to these regions, as discussed in the text. Our residue level associations of NMR peaks with specific results are tentative and do not correspond to confirmed spectral assignments.

appear in some but not all the PrLD spectra. The regions 3 and 5 include crosspeaks between atoms on nearest-neighbor amino acids, most likely residues adjacent to S residues. Regions 4 and 7 correspond to the high-abundance amino acids S and A. The homotypic PrLD fibrils may have a structure like the cryo-EM structure reported earlier (68), in terms of residues involved in the core fibril. In contrast, we detected fewer signals overall in the spectra from αS-seeded and heterotypic fibrils (Fig. 6, *B* and *C*, respectively), suggesting that these structures include smaller (or entirely distinct) regions of PrLD.

αS^{f}-seeded PrLD fibrils cause synaptic dysfunction in primary neuronal cultures

To determine the functional consequences of αS-induced TDP-43 polymorphs, we investigated their effect on synapses. C57BL/6 primary cortical neurons were treated with 1 μM of αS^{f}-seeded PrLD fibrils along with homotypic αS and PrLD fibrils. The monomers of each protein were also used as controls. The cells were fixed after 24 h and immunostained using presynaptic (Synapsin 1) and postsynaptic (PSD95) antibodies (Fig. 7*A*). The cells were then imaged using a confocal microscope and analyzed using the protocols described in the Experimental procedures. The αS^{f}-seeded PrLD fibrils (p = 0.0138), homotypic αS and PrLD fibrils (p = 0.0013), and αS monomers (p = 0.0089) showed reduction in Synapsin 1 density when compared to the untreated cells (Fig. 7*B*). But the reductions were ∼10% to 15% as compared to the untreated cells (Fig. 7*B*). In contrast, a significant reduction in PSD95 density was observed when the neurons were treated with αS^{f}-seeded PrLD fibrils (∼35%; $p < 0.001$), followed by PrLD and αS monomers (∼18%–20%) as compared to the untreated control (Fig. 7*C*). Analysis of the colocalization of the presynaptic and postsynaptic signal density also showed that αS^{f}-seeded PrLD fibrils treated neurons had the greatest reduction compared to untreated cells (∼50%; Fig. 7*D*). This suggests that selectively, αS^{f}-seeded PrLD fibril polymorph is able to reduce the number of functional synapses in primary neurons. In sum, the data indicate that αS^{f}-seeded PrLD fibril polymorph could contribute to synaptic dysfunction.

Discussion

Significant clinical and pathological overlaps observed among neurodegenerative diseases have brought to bear increased attention on understanding the potential cross-interactions between different amyloid proteins. Many amyloid proteins are known to crossinteract with one another both *in vitro* and *in vivo* including Aβ and hIAPP (69–71), αS and tau (72, 73), and αS and Aβ (74, 75). Recently, tau was shown to induce distinct molecular conformations of αS filaments *in vitro*, implicating that heterotypic interactions may generate specific polymorphs and potentially discrete phenotypes (76). However, the involvement of heterotypic aggregates formed as a result of coaggregation of two different proteins to behave as polymorphic strains remains unclear. Compounding this scarcity is the lack of high resolution structures of brain-derived TDP-43 polymorphs. In fact, only a few examples exist that include the cryo-EM structure of TDP-43 PrLD fibrils. For example, TDP-43 fibrils derived from frontal cortex of an ALS patient showed a unique 'double-spiral fold' (77).

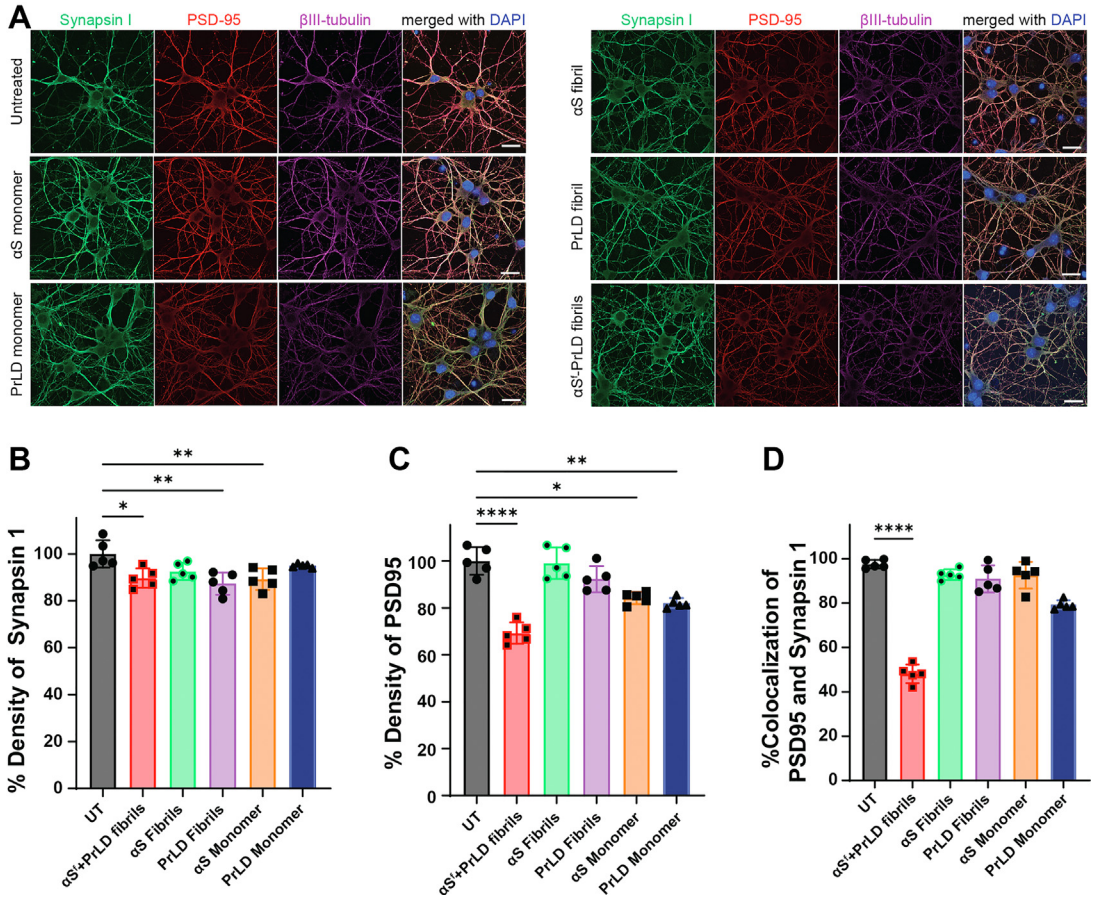

Figure 7. Effect of monomeric and fibrillar αS and TDP-43 PrLD along with αS^f-seeded TDP-43 PrLD fibrils on presynaptic and postsynaptic expression in primary cortical neurons. *A*, representative confocal images of C57BL/6 primary cortical neurons treated with 1 μM monomer (left panel) or fibril (right panel) of α-Synuclein (αS), prion-like domain (PrLD) of TDP-43, or αS fibrils seeded TDP-43 PrLD fibrils (αS^f-PrLD) for 24 h. Cells were fixed and immunostained with presynaptic marker (Synapsin I, *green*), postsynaptic maker (PSD-95, *red*), mature neuronal marker (βIII-tubulin, *magenta*), and merged with nuclear staining (DAPI, *blue*). The scale bar represents 20 μm. *B–D*, quantification of density of presynaptic (*B*), postsynaptic (*C*), and Pearson's colocalization coefficient analysis of the synaptic proteins (*D*) in αS, PrLD, or αS^f-PrLD-treated primary neurons using Imaris software. Each treatment group was randomly imaged in five different regions of interest and performed in triplicate. Image analysis was calculated by one-way ANOVA with Tukey's multiple comparison. Bar graphs represent the value of mean ± SD. *$p < 0.05$, **$p < 0.01$, ****$p < 0.0001$. DAPI, 4′,6-diamidino-2-phenylindole.

This was different from the cryo-EM structure of PrLD fibrils generated *in vitro* (68). In addition, two different amyloid forming segments of TDP-43, SegA (residue 311–360), and SegB A315E (386-331) revealed four different polymorphs (44). TDP-43 strains have also been isolated from FTLD-TDP brain tissues, which induce the formation of morphologically distinct aggregates in cells, and induce distinct morphological and subcellular distribution of TDP-43 pathology in transgenic mice (45). Although these studies showed TDP-43 polymorphs both *in vitro* and *in vivo*, TDP-43 strains in copathologies are not investigated so far. In our previous study, we discovered that αS monomers, oligomers, and fibrils are able to promote PrLD fibrillization (52), further providing a possible molecular mechanism by which the two proteins may interact with one another. This current report advances these findings by showing that the two proteins indeed form colocalized cytoplasmic foci in SH-SY5Y neuroblastoma cells. More importantly, the data unequivocally show that depending on the nature of the αS seeds, that is, whether they are monomers or fibrils, conformationally distinct polymorphs of PrLD are generated. However, it is interesting to observe that addition of αS (monomers or fibrils) seems to destabilize heterotypic PrLD fibril polymorphs by making them more amorphous (evident from PK digestion and temperature stability data). Equimolar incubation of both monomers generates fibrils in which the proteins retain their equimolar composition suggesting 'hybrid' fibrils (52). Au-nanoparticle labeling and TEM of PrLD–αS hybrid fibrils shown here unequivocally suggests integration of αS within the PrLD fibrils. Although it is clear that hybrid fibrils are less stable and more susceptible toward enzymatic digestion, they show residue-level differences in solid-state NMR (ssNMR), suggesting a different structure as compared to either αS^f-seeded or αS^f-unseeded PrLD. Fibril polymorphism has also been made evident by differences in intrinsic tryptophan fluorescence and dye-binding assays. This may be due to different fibrillar structure; for example, length or width of fibrils, degree of twisting, and crossover distance. More importantly, such differences may alter degree of accessibility to dye-binding regions or completely mask the dye-binding surfaces that are revealed by total fluorescence intensity or change in emission maxima (59, 78). Despite being less stable than homotypic PrLD fibrils, the αS^f-seeded PrLD

fibrils show significantly different synaptic effect in primary neurons, suggesting amorphous polymorph may functionally be more deleterious *in vivo*.

It is important to distinguish the differences between the cross-seeding and heterotypic coaggregation. As discussed throughout the article, several examples of cross-seeding interactions among amyloid proteins exist. Typically, cross-seeding occurs when a preformed seed of one amyloid protein enhances the aggregation of a second amyloid protein. Such a cross-seeding may result in fibrils that are similar or dissimilar to homotypic fibrils without the influence of the second amyloid protein seed. On the other hand, coaggregation is a process of synergistic aggregation of two different amyloid protein monomers toward heterotypic hybrid fibrils containing both proteins. Hybrid heterotypic aggregates thus far have not been observed among amyloid proteins except for a select few atypical amyloid systems (79–82). PrLD–αS hybrid fibrils shown here and in our previous study (52) form the first among the class of hybrid heterotypic amyloid fibrils. Furthermore, the results presented here suggest that both heterotypic PrLD fibrils (cross-seeded or coaggregated with αS) have different structures and biophysical properties.

Among the two modes of crossinteractions of PrLD with αS, that is, αS monomers or $αS^f$, the latter is more pathologically relevant as pre-existing Lewy bodies can seed TDP-43 aggregates in the cytoplasm. Although, reverse phenomenon involving $PrLD^f$ seeding αS monomers could also be equally relevant and interesting, this was not investigated because our earlier data demonstrated that seeding of $αS^f$ to PrLD monomers is far more efficient than $PrLD^f$ seeding αS monomers, suggesting conformational selectivity in seeding (83–85). The data presented here establish that aggregation dynamics and structures of PrLD fibrils grown under the influence of αS are different from the homotypic PrLD fibrils. Importantly, polymorphism seems to be correlated with pathological changes in primary neurons. However, several questions still remain less understood. For example, how PrLD fibril polymorph generated *via* templated seeding of $αS^f$ is different from those generated by coaggregating monomers of PrLD and αS (PrLD–αS hybrid fibrils) or homotypic PrLD fibrils? Similarly, it will be interesting to understand how PrLD–αS hybrid fibrils are organized; are the cross β-sheets interdigitated β-strands of PrLD and αS or are they formed as block polymers by epitaxial growth of the two fibrils? In-depth investigations in the future will enable better insights into the structures of PrLD fibril polymorphs, which may uncover molecular basis of phenotype emergence in comorbid neurodegenerative diseases.

Experimental procedures

Recombinant expression and purification of unlabeled PrLD, αS, ^{13}C-labeled PrLD and ^{15}N-labeled αS

Recombinant expression and purification of both unlabeled and $^{13}C/^{15}N$-labeled TDP-43 PrLD and αS was carried out as described previously (52). For TDP-43 PrLD, N-terminal hexahistidine tag fused construct (Addgene plasmid #98669) with a tobacco etch virus (TEV) cleavage site was expressed in BL21 Star (DE3) cells and purified using Ni-NTA affinity chromatography. Briefly, cells expressing unlabeled and labeled TDP-43 PrLD were resuspended in lysis buffer (20 mM Tris, 500 mM NaCl, 5 mM imidazole, 6M urea, 0.5 mM PMSF, pH 8.0), sonicated, and centrifuged. The supernatant was incubated with the Ni-NTA beads and washed using wash buffers each containing 15 mM and 30 mM imidazole in buffer containing 20 mM Tris, 500 mM NaCl, 6M urea, pH 8.0, to remove nonspecifically bound proteins. Protein was eluted in 150 mM imidazole containing elution buffer followed by dialysis in 20 mM Tris buffer, 500 mM NaCl, 2M urea, pH 8.0, concentrated, and stored at -80 °C. For experiments, protein was thawed in ice and desalted using Sephadex G-25 HiTrap desalting column (Cytiva) in 20 mM MES buffer pH 6.0. Protein concentration was determined using UV spectrometer (extinction coefficient 19,480 M^{-1} cm^{-1}). Both unlabeled and ^{15}N labeled recombinant αS was expressed as N terminus hexahistidine tag followed by thrombin cleavage site in BL21 (DE3) cells. Protein was purified using Ni-NTA affinity chromatography, eluted in elution buffer containing 250 mM imidazole, dialyzed in nanopore water to remove imidazole, concentrated using 10 kDa centrifugal filter (Thermo fisher), and stored at -80 °C. Prior to the experiments, protein was thawed in ice and incubated for 30 min with 40 mM NaOH to disaggregate the oligomers and subjected to size-exclusion chromatography using Superdex-200 column in 20 mM MES buffer pH 6.0. Protein concentration was determined using UV spectrometer using extinction coefficient 5960 M^{-1} cm^{-1}.

Labeling of monomeric αS

For cell culture studies, αS was fluorescently labeled using HiLyte Fluor 405 succinimidyl ester (Anaspec). Monomeric αS in 20 mM MES buffer pH 6.0 was incubated with 3 M excess of dye and incubated at 4 °C for 16 h. Excess dye was removed using Sephadex G-25 HiTrap desalting column (Cytiva) for two times and protein was eluted in sterile 20 mM Tris buffer pH 7.5. The protein was used as such for internalization assays.

Cell growth, transfection, and colocalization analysis

Colocalization analysis of αS and TDP-43 PrLD was carried out in SH-SY5Y neuroblastoma cells (ATCC) maintained at 37 °C and 5.5% CO_2 in Dulbecco's modified Eagle's medium and F-12 (1:1) media containing 10% fetal bovine serum and 1% penicillin/streptomycin (Thermo Fisher Scientific). At first, transfection reagent was prepared by mixing 9 μl of Opti-MEM, 100 ng of TDP-43 PrLD plasmid (sBFP2-PrLD) and TransIT-X2 dynamic delivery system, Mirius (0.3 μL). The mixture was incubated for 20 min prior to transfection in cells with confluency greater than 70% that are grown by seeding 45,000 cells/well in 96-well glass bottom plates (Cellvis). After 24 h, media containing transfection reagent was replaced, washed for two times with warm fresh media, and incubated with approximately 500 nM Hilyte-532–labeled recombinant αS monomers. Cells were further incubated for 24 h and media

containing αS monomers was replaced with fresh media. Cells were stained with nuclear marker (NucSpot Live 650, Biotium) and imaged using Leica STELLARIS-DMI8 microscope at 40× magnification. All the acquired images were processed using Adobe illustrator software (Adobe Inc) and cytoplasmic puncta from the respective images were counted using ImageJ software (https://imagej.nih.gov/ij/index.html).

Preparation of homotypic and heterotypic fibrils

Both labeled and unlabeled fibrils samples were prepared for different biophysical studies. For ssNMR, homotypic fibrils of ^{13}C-labeled TDP-43 PrLD, hybrid fibrils containing ^{13}C TDP-43 PrLD and ^{15}N αS, and αS^{f}-seeded ^{13}C-labeled TDP-43 PrLD fibrils were used. Homotypic ^{13}C labeled-TDP-43 PrLD fibrils were prepared by incubating 20 μM ^{13}C-labeled TDP-43 PrLD monomers for 7 days. Hybrid fibrils were prepared by mixing 20 μM ^{13}C TDP-43 PrLD and ^{15}N αS at 1:1 stoichiometry and incubating for 7 days. αS^{f}-seeded TDP-43 PrLD fibrils were prepared by incubating 2 μM αS sonicated fibrils with 20 μM ^{13}C TDP-43 PrLD for 7 days. All the samples were incubated under quiescent conditions in 20 mM MES buffer, 0.01% sodium azide, pH 6.0 at 37 °C. Fibrils from respective reaction were harvested by centrifuging at 20,000×*g* for 20 min, washed, and centrifuged fibrils pellets were subjected for ssNMR studies. For other studies, unlabeled fibrils were prepared and resuspended in sterile water or buffer prior to the experiment. αS fibrils were prepared by incubating 5 mg of αS monomers with 150 mM NaCl and 0.01% sodium azide in 20 mM Tris buffer pH 8.0 at 37 °C and 600 rpm for 10 to 14 days. The fibrils were centrifuged at 18,000×*g* for 20 min, washed, and resuspended in water or buffer of choice. αS-sonicated fibrils were generated by sonicating resuspended fibrils using Misonix XL-2000 sonicator for seven cycles each with 30 s burst and 1 min rest at 35% intensity, incubated on ice for 30 min prior to incubation with TDP-43 PrLD.

Au-nanoparticle labeling and TEM

All the unlabeled fibrils were prepared as described earlier. Au-nanoparticle–labeled PrLD fibrils were prepared by mixing 5 μM his-tagged PrLD monomers with 20 μM untagged PrLD monomers and incubated under quiescent condition at 37 °C. Moreover, nanogold-labeled hybrid fibrils were prepared by incubating 20 μM untagged PrLD monomers with 5 μM his-tagged αS monomers and 15 μM untagged αS monomers under quiescent condition at 37 °C. Fibrils were harvested by centrifugation and resuspended in ultrapure water. These were directly incubated with 5 nm Ni-NTA-Nanogold (Nanoprobes Inc) stock solution at 1:20 v/v dilution. Freshly prepared nanogold-labeled and unlabeled fibrils stock solution was diluted to 1 μM in ultrapure water prior to TEM imaging. All samples were then applied onto ultrathin carbon film supported by a lacey carbon film on 400 mesh copper grids (Ted Pella Inc) for 2 min. Nanogold-labeled samples had an additional wash step of spotting 5 ml of ultrapure water onto the grid for 1 min two times. Samples were then negatively stained with 2% uranyl acetate for 1 min. TEM grids were analyzed using a Hitachi HT-7700 TEM.

Intrinsic tryptophan fluorescence and dye-binding assays

Intrinsic tryptophan fluorescence and dye binding of monomers, homotypic and heterotypic fibrils were carried out in Cary Eclipse spectrometer (Varian Inc) in scan mode. Stock solution of ANS was prepared in water, whereas DCVJ and curcumin were prepared in 95% ethanol. In intrinsic tryptophan fluorescence, samples were equilibrated for 1 min and spectra were collected by setting the excitation and emission wavelength at 280 nm and 300 to 450 nm, respectively. For ANS, samples were diluted in 100 μM ANS, equilibrated for 1 min and spectra were collected by setting the excitation and emission wavelength of 388 nm and 400 to 650 nm, respectively. For DCVJ, samples were diluted in 10 μM DCVJ, equilibrated for 1 min, before measuring the fluorescence at excitation and emission wavelength of 433 nm and 450 to 650 nm, respectively. Similarly, curcumin fluorescence was measured by incubating the samples in 5 μM curcumin followed by 1 min equilibration. Fluorescence spectra were collected in excitation and emission wavelength of 430 nm and 470 to 600 nm, respectively. All the samples were used at 2 μM final concentration in 20 mM MES buffer pH 6.0. The shift in fluorescence emission wavelength maxima was calculated by subtracting the emission wavelength maxima of samples to TDP-43 PrLD monomers. Moreover, percentage change in intensity was calculated by subtracting the integrated area under the curve of samples to TDP-43 PrLD monomers.

PK digestion

Homotypic and heterotypic fibrils (∼4 μg) formed by αS and TDP-43 PrLD were resuspended in sterile water and subjected to digestion using 280 ng of PK (Ambion, Inc) diluted from a stock of 20 mg/ml in sterile water. All the reactions were carried out by shaking at 200×*g* at 37 °C. Reactions were quenched at 10, 20, 30, and 40 min, respectively, using 0.5 mM PMSF. Finally, aliquots of reactions were mixed with nonreducing laemmli sample buffer (4×) and subjected to SDS-PAGE. Gel was stained using Pierce silver stain kit (Thermo Fisher scientific) as per manufacturer's protocol and imaged on a GelDoc molecular imager (Bio-Rad).

MALDI-TOF spectrometry

PK digestion of monomers, homotypic and heterotypic fibrils (1 μg) was carried out as described before. Samples for MALDI-TOF were prepared by mixing 1 μl of the digested fibrils with equal volume of sinapinic acid prepared in 1:1 acetonitrile/water and 0.1% TFA. The sample was spotted on the MSP 96 MALDI plate (Bruker Daltonics). Spectra were collected by maintaining the laser power at 70% and analyzed using flex analysis. All the data were processed using OriginPro 8.5 (OriginLab Inc).

CD melting

SDS-induced temperature melt of TDP-43 PrLD monomers or homotypic fibrils, hybrid fibrils, and αS^{f}-seeded PrLD fibrils was carried out on a Jasco J-815 spectrometer. The fibrils were

resuspended in water and spectra were collected in 10 mm pathlength cuvette at standard sensitivity with scan rate of 50 nm/min, 8 s DIT, 1 nm bandwidth, and 0.1 nm data pitch. For stability analysis, 1% w/v SDS was added to the samples, immediately followed by temperature interval measurement by collecting the spectra at every 5 °C temperature interval from 20 °C to 90 °C. The data were normalized for mean residual ellipticity and ellipticity difference between 208 nm and 218 nm was calculated. The ellipticity difference, as an indicative of α-helical or β-sheet structure, was plotted against the temperature and fit using the Sigmoidal Boltzmann function (see equation below) in Origin 8.5.

$$y = \frac{A_1 - A_2}{1 + e^{(x - x_0)/dx}} + A_2$$

ssNMR

Fibrils were packed into Bruker 3.2 mm NMR rotors *via* ultracentrifugation at 4 °C and 150,000*g* for 30 min using Beckman Optima XPN-100 fitted with a SW-41 Ti swinging-bucket rotor and Ultra-Clear tubes. NMR spectra were collected on a 11.75 T magnet (500 MHz 1H NMR frequency) using a Bruker spectrometer and a 3.2 mm Bruker Low-E 1H/13C/15N NMR probe. Two-dimensional 13C-13C NMR spectra were collected using the two-dimensional dipolar assisted rotational resonance NMR technique at 10 kHz magic angle spinning speed with a mixing time of 50 ms. A 1H radiofrequency field of 100 kHz was used. Signal averaging of all the spectra in Fig. 6 required approximately 24 h. This technique produces off-diagonal peaks (crosspeaks) that mostly correspond to interactions between 13C atoms within the same amino acid (64, 86, 87).

Primary neuron isolation and cell treatment

This study was conducted in a facility approved by the American Association for the Accreditation of Laboratory Animal Care. All procedures were performed in accordance with recommendations in the Guide for the Care and Use of Laboratory Animals of the National Institutes of Health. Our protocol was approved by the Institutional Animal care and Use Committee of the University of Texas Medical Branch (UTMB). Primary cortical neuronal cultures were prepared and maintained as described previously (62, 88–90). Briefly, cortices were isolated from C57BL/6 mice (Jackson Laboratory; 000664) during embryonic day 13 to 16. Brain tissues were digested using Accutase solution (Sigma) followed by gentle trituration with a fire-polished glass pasture pipet. Dissociated cells were plated at a density of 1.6×10^5 cells/ml on poly-L-lysine–coated coverslips. Culture media contains neurobasal medium (Gibco; 12348017) supplemented with 2% B-27 Plus supplement (Gibco; A3582801), 0.5 mM GlutaMax (Gibco; 35050-061), 10,000 units/ml penicillin, 10,000 μg/ml streptomycin, and 25 μg/ml amphotericin B (Gibco; 15240062). Half of the media was changed every 3 to 4 days. On 10 days *in vitro*, cells were treated with monomers or fibrils of α-synuclein, TDP-43 PrLD, or αS^f-seeded PrLD fibrils at 1 μM for 24 h. Buffers used in samples preparation were the vehicle control in all experiment.

Immunofluorescence, confocal microscopy, and imaging analysis

After cell treatments, primary neurons were gently washed three times with 1× PBS. Formaldehyde solution 4% (Sigma) was used for fixation for 15 min at room temperature (RT) followed by three washes. Cells were permeabilized using 0.25% Triton X-100 (Sigma) in 1× PBS for 10 min and blocked for 30 min at RT in blocking buffer. Cells were then incubated with primary antibodies diluted in blocking buffer overnight at 4 °C. Primary antibodies used include mouse anti-βIII-tubulin (1:1000, Abcam; ab78078), rabbit anti-Synapsin I (1:1000, Abcam; ab8), or rabbit anti-PSD95 (1:1000, Abcam; ab18258). On the next day, cells were washed and incubated with secondary antibodies (1:700, Life Technologies) for 1 h at RT in the dark. After three washes, cells were mounted with Prolong Gold antifade reagent with 4′,6-diamidino-2-phenylindole. All samples were examined with 63× objective of a Zeiss LSM 880 confocal microscope using 405 nm diode laser and argon laser 458/488/514 nm. To build the z-stack, 17 stacks/0.37 to 0.41 μm optimal thickness were captured. Each treatment condition was randomly imaged in five different regions of interest and performed in duplicate. Neuron-specific presynaptic and postsynaptic signals were analyzed using Imaris software (Oxford Instruments Inc) as previously described (91). Briefly, for each image, presynaptic (Synapsin-1) and postsynaptic (PSD-95) channels were filtered based on neuronal surface and discrete quantitative "spots" were created. Once presynaptic and postsynaptic spots were detected, the distance threshold to identify colocalized spots was set to 1 mm, providing for an estimate of synapse number (92–94). The number of colocalized spots were normalized to the untreated. Statistical analysis was performed in GraphPad Prism 9 (GraphPad Software Inc) using one-way ANOVA followed by Tukey's Test. Results were considered statistically significant at $p < 0.05$.

Data availability

Most of data presented in the article are self-contained within the article. Raw MALDI-TOF data have been appended in the supplementary information. Additional data on NMR, confocal microscopy, and biophysical experiments are available upon request. Please contact the corresponding authors, Drs. Vijay Rangachari (Vijay.rangachari@usm.edu) or Anant Paravastu (anant.paravastu@chbe.gatech.edu).

Supporting information—This article contains supporting information.

Acknowledgments—The authors acknowledge NMR facility at Georgia Tech and Robert P. Apkarian Integrated Electron Microscopy Core at Emory. The authors would also like to thank Dr Jonathan Lindner for his gracious help with the confocal microscope use and troubleshooting.

Author contributions—V. R. conceptualization; A. K. P., R. K., and S. D. validation; V. R., A. K. P., N. B., N. P. and L. F. formal analysis; R. K., S. D., A. S. R., N. B., N. P. and L. F. investigation; S. D. and A. S. R. data curation; V. R., A. K. P., S. D., and A. S. R. writing–original draft; V. R., A. K. P., S. D., A. S. R., N. B., N. P. and L. F. writing–review & editing.

Funding and additional information—The authors would like to thank the following agencies for financial support: National Institute of Aging, United States (1R56AG062292-01 (to V. R.); AG054025, RF1AG077484 (to R. K.) and RF1AG073434-01A1 (to A. K. P.), the National Institute on Minority Health and Health Disparities, United States (RF1AG073434-01A1; to A. K. P.), and the National Science Foundation, United States (NSF CBET 1802793) to V. R.. The authors also thank the National Center for Research Resources (5P20RR01647-11) and the National Institute of General Medical Sciences (8 P20 GM103476-11) from the National Institutes of Health for funding through INBRE for the use of their core facilities, and the National Science Foundation (NSF MRI 2019023) for STED confocal microscope facility. The content is solely the responsibility of the authors and does not necessarily represent the official views of the National Institutes of Health.

Conflict of interests—The authors declare that they have no conflicts of interest with the contents of this article.

Abbreviations—The abbreviations used are: ANS, 8-anilinonaphthalene-1-sulfonic acid; DCVJ, 9-(dicyano-vinyl) julolidine; LBD, Lewy body disease; ssNMR, solid-state NMR; TEM, transmission electron microscopy.

References

1. Armstrong, R. A., Lantos, P. L., and Cairns, N. J. (2008) What determines the molecular composition of abnormal protein aggregates in neurodegenerative disease? *Neuropathology* **28**, 351–365
2. Davis, A. A., Leyns, C. E., and Holtzman, D. M. (2018) Intercellular spread of protein aggregates in neurodegenerative disease. *Annu. Rev. Cell Dev. Biol.* **34**, 545–568
3. Seeman, P., and Seeman, N. (2011) Alzheimer's disease: β-amyloid plaque formation in human brain. *Synapse* **65**, 1289–1297
4. Kovacs, G. G. (2016) Molecular pathological classification of neurodegenerative diseases: Turning towards precision medicine. *Int. J. Mol. Sci.* **17**, 189–222
5. Kawakami, I., Arai, T., and Hasegawa, M. (2019) The basis of clinicopathological heterogeneity in TDP-43 proteinopathy. *Acta Neuropathol.* **138**, 751–770
6. Walker, L. C. (2016) Proteopathic strains and the heterogeneity of neurodegenerative diseases. *Annu. Rev. Genet.* **50**, 329–346
7. Lau, A., So, R. W., Lau, H. H., Sang, J. C., Ruiz-Riquelme, A., Fleck, S. C., *et al.* (2020) α-Synuclein strains target distinct brain regions and cell types. *Nat. Neurosci.* **23**, 21–31
8. Armstrong, R. A., Lantos, P. L., and Cairns, N. J. (2005) Overlap between neurodegenerative disorders. *Neuropathology* **25**, 111–124
9. Ahmed, R. M., Devenney, E. M., Irish, M., Ittner, A., Naismith, S., Ittner, L. M., *et al.* (2016) Neuronal network disintegration: Common pathways linking neurodegenerative diseases. *J. Neurol. Neurosurg. Psychiatry* **87**, 1234–1241
10. Das, S., Zhang, Z., and Ang, L. C. (2020) Clinicopathological overlap of neurodegenerative diseases: a comprehensive review. *J. Clin. Neurosci.* **78**, 30–33
11. Duda, J. E., Giasson, B. I., Mabon, M. E., Miller, D. C., Golbe, L. I., Lee, V. M.-Y., *et al.* (2002) Concurrence of α-synuclein and tau brain pathology in the contursi kindred. *Acta Neuropathol.* **104**, 7–11
12. Lee, V. M., Giasson, B. I., and Trojanowski, J. Q. (2004) More than just two peas in a pod: Common amyloidogenic properties of tau and α-synuclein in neurodegenerative diseases. *Trends Neurosci.* **27**, 129–134
13. Nakashima-Yasuda, H., Uryu, K., Robinson, J., Xie, S. X., Hurtig, H., Duda, J. E., *et al.* (2007) Co-morbidity of TDP-43 proteinopathy in Lewy body related diseases. *Acta Neuropathol.* **114**, 221–229
14. Crews, L., Tsigelny, I., Hashimoto, M., and Masliah, E. (2009) Role of synucleins in Alzheimer's disease. *Neurotox. Res.* **16**, 306–317
15. Dupiereux, I., Zorzi, W., Quadrio, I., Perret-Liaudet, A., Kovacs, G. G., Heinen, E., *et al.* (2009) Creutzfeldt-jakob, parkinson, lewy body dementia and alzheimer diseases: From diagnosis to therapy. *Cent. Nerv. Syst. Agents Med. Chem.* **9**, 2–11
16. Irwin, D. J., Lee, V. M.-Y., and Trojanowski, J. Q. (2013) Parkinson's disease dementia: Convergence of α-synuclein, tau and amyloid-β pathologies. *Nat. Rev. Neurosci.* **14**, 626–636
17. Chornenkyy, Y., Fardo, D. W., and Nelson, P. T. (2019) Tau and TDP-43 proteinopathies: Kindred pathologic cascades and genetic pleiotropy. *Lab. Investig.* **99**, 993–1007
18. Visanji, N. P., Lang, A. E., and Kovacs, G. G. (2019) Beyond the synucleinopathies: Alpha synuclein as a driving force in neurodegenerative comorbidities. *Transl. Neurodegener.* **8**, 1–13
19. Karanth, S., Nelson, P. T., Katsumata, Y., Kryscio, R. J., Schmitt, F. A., Fardo, D. W., *et al.* (2020) Prevalence and clinical phenotype of quadruple misfolded proteins in older adults. *JAMA Neurol.* **77**, 1299–1307
20. Williams, T., Sorrentino, Z., Weinrich, M., Giasson, B. I., and Chakrabarty, P. (2020) Differential cross-seeding properties of tau and α-synuclein in mouse models of tauopathy and synucleinopathy. *Brain Commun.* **2**, 102270–102283
21. Galpern, W. R., and Lang, A. E. (2006) Interface between tauopathies and synucleinopathies: A tale of two proteins. *Ann. Neurol.* **59**, 449–458
22. Dickson, D. W., Kouri, N., Murray, M. E., and Josephs, K. A. (2011) Neuropathology of frontotemporal lobar degeneration-tau (FTLD-tau). *J. Mol. Neurosci.* **45**, 384–389
23. Obi, K., Akiyama, H., Kondo, H., Shimomura, Y., Hasegawa, M., Iwatsubo, T., *et al.* (2008) Relationship of phosphorylated α-synuclein and tau accumulation to Aβ deposition in the cerebral cortex of dementia with Lewy bodies. *Exp. Neurol.* **210**, 409–420
24. Goedert, M., Falcon, B., Clavaguera, F., and Tolnay, M. (2014) Prion-like mechanisms in the pathogenesis of tauopathies and synucleinopathies. *Curr. Neurol. Neurosci. Rep.* **14**, 1–11
25. de Boer, E. M. J., Orie, V. K., Williams, T., Baker, M. R., De Oliveira, H. M., Polvikoski, T., *et al.* (2021) TDP-43 proteinopathies: A new wave of neurodegenerative diseases. *J. Neurol. Neurosurg. Psychiatry* **92**, 86–95
26. Yokota, O., Davidson, Y., Arai, T., Hasegawa, M., Akiyama, H., Ishizu, H., *et al.* (2010) Effect of topographical distribution of α-synuclein pathology on TDP-43 accumulation in lewy body disease. *Acta Neuropathol.* **120**, 789–801
27. Uemura, M. T., Robinson, J. L., Cousins, K. A., Tropea, T. F., Kargilis, D. C., McBride, J. D., *et al.* (2022) Distinct characteristics of limbic-predominant age-related TDP-43 encephalopathy in lewy body disease. *Acta Neuropathol.* **143**, 15–31
28. Sun, Y., and Chakrabartty, A. (2017) Phase to phase with TDP-43. *Biochem* **56**, 809–823
29. Gao, J., Wang, L., Huntley, M. L., Perry, G., and Wang, X. (2018) Pathomechanisms of TDP-43 in neurodegeneration. *J. Neurochem.* **146**, 7–20
30. Ratti, A., and Buratti, E. (2016) Physiological functions and pathobiology of TDP-43 and FUS/TLS proteins. *J. Neurochem.* **138**, 95–111
31. Birsa, N., Bentham, M. P., and Fratta, P. (2020) Cytoplasmic functions of TDP-43 and FUS and their role in ALS. *Semin. Cell Dev. Biol.* **99**, 193–201
32. Dammer, E. B., Fallini, C., Gozal, Y. M., Duong, D. M., Rossoll, W., Xu, P., *et al.* (2012) Coaggregation of RNA-binding proteins in a model of TDP-43 proteinopathy with selective RGG motif methylation and a role for RRM1 ubiquitination. *PLoS one* **7**, e38658
33. Zhang, Y.-J., Xu, Y.-F., Cook, C., Gendron, T. F., Roettges, P., Link, C. D., *et al.* (2009) Aberrant cleavage of TDP-43 enhances aggregation and cellular toxicity. *Proc. Natl. Acad. Sci.* **106**, 7607–7612

34. Hasegawa, M., Arai, T., Nonaka, T., Kametani, F., Yoshida, M., Hashizume, Y., *et al.* (2008) Phosphorylated TDP-43 in frontotemporal lobar degeneration and amyotrophic lateral sclerosis. *Ann. Neurol.* **64**, 60–70
35. Inukai, Y., Nonaka, T., Arai, T., Yoshida, M., Hashizume, Y., Beach, T. G., *et al.* (2008) Abnormal phosphorylation of Ser409/410 of TDP-43 in FTLD-U and ALS. *FEBS Lett.* **582**, 2899–2904
36. Suk, T. R., and Rousseaux, M. W. (2020) The role of TDP-43 mislocalization in amyotrophic lateral sclerosis. *Mol. Neurodegener.* **15**, 1–16
37. Feneberg, E., Charles, P. D., Finelli, M. J., Scott, C., Kessler, B. M., Fischer, R., *et al.* (2021) Detection and quantification of novel C-terminal TDP-43 fragments in ALS-TDP. *Brain Pathol.* **31**, e12923
38. Berning, B. A., and Walker, A. K. (2019) The pathobiology of TDP-43 C-terminal fragments in ALS and FTLD. *Front. Neurosci.* **13**, 335–362
39. Ruz, C., Alcantud, J. L., Vives Montero, F., Duran, R., and Bandres-Ciga, S. (2020) Proteotoxicity and neurodegenerative diseases. *Int. J. Mol. Sci.* **21**, 5646–5671
40. Jia, C., Ma, X., Liu, Z., Gu, J., Zhang, X., Li, D., *et al.* (2019) Different heat shock proteins bind α-Synuclein with distinct mechanisms and synergistically prevent its amyloid aggregation. *Front. Neurosci.* **13**, 1124–1136
41. Tian, T., Huang, C., Tong, J., Yang, M., Zhou, H., and Xia, X.-G. (2011) TDP-43 potentiates alpha-synuclein toxicity to dopaminergic neurons in transgenic mice. *Int. J. Biol. Sci.* **7**, 234–243
42. Shen, L., Wang, C., Chen, L., Leung, K. L., Lo, E., Lakso, M., *et al.* (2020) TDP-1/TDP-43 potentiates human α-Synuclein (HASN) neurodegeneration in caenorhabditis elegans. *Biochim. Biophys. Acta Mol. Basis Dis.* **1866**, 165876–16590
43. Nonaka, T., Masuda-Suzukake, M., and Hasegawa, M. (2018) Molecular mechanisms of the co-deposition of multiple pathological proteins in neurodegenerative diseases. *Neuropathol* **38**, 64–71
44. Cao, Q., Boyer, D. R., Sawaya, M. R., Ge, P., and Eisenberg, D. S. (2019) Cryo-EM structures of four polymorphic TDP-43 amyloid cores. *Nat. Struct. Mol. Biol.* **26**, 619–627
45. Porta, S., Xu, Y., Lehr, T., Zhang, B., Meymand, E., Olufemi, M., *et al.* (2021) Distinct brain-derived TDP-43 strains from FTLD-TDP subtypes induce diverse morphological TDP-43 aggregates and spreading patterns *in vitro* and *in vivo*. *Neuropathol. Appl. Neurobiol.* **47**, 1033–1049
46. Mehra, S., Gadhe, L., Bera, R., Sawner, A. S., and Maji, S. K. (2021) Structural and functional insights into α-synuclein fibril polymorphism. *Biomolecules* **11**, 1419–1454
47. Colletier, J.-P., Laganowsky, A., Landau, M., Zhao, M., Soriaga, A. B., Goldschmidt, L., *et al.* (2011) Molecular basis for amyloid-β polymorphism. *Proc. Natl. Acad. Sci.* **108**, 16938–16943
48. Wegmann, S., Jung, Y. J., Chinnathambi, S., Mandelkow, E.-M., Mandelkow, E., and Muller, D. J. (2010) Human Tau isoforms assemble into ribbon-like fibrils that display polymorphic structure and stability. *J. Biol. Chem.* **285**, 27302–27313
49. Sengupta, U., Guerrero-Muñoz, M. J., Castillo-Carranza, D. L., Lasagna-Reeves, C. A., Gerson, J. E., Paulucci-Holthauzen, A. A., *et al.* (2015) Pathological interface between oligomeric alpha-synuclein and tau in synucleinopathies. *Biol. Psychiatry* **78**, 672–683
50. Ivanova, M. I., Lin, Y., Lee, Y.-H., Zheng, J., and Ramamoorthy, A. (2021) Biophysical processes underlying cross-seeding in amyloid aggregation and implications in amyloid pathology. *Biophys. Chem.* **269**, 106507–106523
51. Louros, N., Schymkowitz, J., and Rousseau, F. (2022) Heterotypic amyloid interactions: clues to polymorphic bias and selective cellular vulnerability? *Curr. Opin. Struct. Biol.* **72**, 176–186
52. Dhakal, S., Wyant, C. E., George, H. E., Morgan, S. E., and Rangachari, V. (2021) Prion-like C-terminal domain of TDP-43 and α-Synuclein interact synergistically to generate neurotoxic hybrid fibrils. *J. Mol. Biol.* **433**, 166953–166959
53. Lee, H.-J., Suk, J.-E., Bae, E.-J., Lee, J.-H., Paik, S. R., and Lee, S.-J. (2008) Assembly-dependent endocytosis and clearance of extracellular a-synuclein. *Int. J. Biochem. Cel. Biol.* **40**, 1835–1849
54. Bhopatkar, A. A., Dhakal, S., Abernathy, H. G., Morgan, S. E., and Rangachari, V. (2022) Charge and redox states modulate granulin—TDP-43 coacervation toward phase separation or aggregation. *Biophys. J.* **121**, 2107–2126
55. Fagerquist, C. K., Sultan, O., and Carter, M. Q. (2012) Possible evidence of amide bond formation between sinapinic acid and lysine-containing bacterial proteins by matrix-assisted laser desorption/ionization (MALDI) at 355 nm. *J. Am. Soc. Mass Spectrom.* **23**, 2102–2114
56. Bolognesi, B., Kumita, J. R., Barros, T. P., Esbjorner, E. K., Luheshi, L. M., Crowther, D. C., *et al.* (2010) ANS binding reveals common features of cytotoxic amyloid species. *ACS Chem. Biol.* **5**, 735–740
57. Kremer, J. J., Pallitto, M. M., Sklansky, D. J., and Murphy, R. M. (2000) Correlation of β-amyloid aggregate size and hydrophobicity with decreased bilayer fluidity of model membranes. *Biochem* **39**, 10309–10318
58. Rao, P. P., Mohamed, T., Teckwani, K., and Tin, G. (2015) Curcumin binding to beta amyloid: A computational study. *Chem. Biol. Drug Des.* **86**, 813–820
59. Saha, J., Dean, D. N., Dhakal, S., Stockmal, K. A., Morgan, S. E., Dillon, K. D., *et al.* (2021) Biophysical characteristics of lipid-induced Aβ oligomers correlate to distinctive phenotypes in transgenic mice. *FASEB J.* **35**, e21318
60. Guo, J. L., Covell, D. J., Daniels, J. P., Iba, M., Stieber, A., Zhang, B., *et al.* (2013) Distinct α-synuclein strains differentially promote tau inclusions in neurons. *Cell* **154**, 103–117
61. Kushnirov, V. V., Dergalev, A. A., and Alexandrov, A. I. (2020) Proteinase K resistant cores of prions and amyloids. *Prion* **14**, 11–19
62. Sengupta, U., Puangmalai, N., Bhatt, N., Garcia, S., Zhao, Y., and Kayed, R. (2020) Polymorphic α-synuclein strains modified by dopamine and docosahexaenoic acid interact differentially with tau protein. *Mol. Neurobiol.* **57**, 2741–2765
63. Conicella, A. E., Zerze, G. H., Mittal, J., and Fawzi, N. L. (2016) ALS mutations disrupt phase separation mediated by α-helical structure in the TDP-43 low-complexity C-terminal domain. *Structure* **24**, 1537–1549
64. Takegoshi, K., Nakamura, S., and Terao, T. (2001) 13C–1H dipolar-assisted rotational resonance in magic-angle spinning NMR. *Chem. Phys. Lett.* **344**, 631–637
65. Pines, A., Gibby, M. G., and Waugh, J. (1973) Proton-enhanced NMR of dilute spins in solids. *J. Chem. Phys.* **59**, 569–590
66. Helmus, J. J., Surewicz, K., Nadaud, P. S., Surewicz, W. K., and Jaroniec, C. P. (2008) Molecular conformation and dynamics of the Y145Stop variant of human prion protein in amyloid fibrils. *Proc. Natl. Acad. Sci.* **105**, 6284–6289
67. Fritzsching, K., Yang, Y., Schmidt-Rohr, K., and Hong, M. (2013) Practical use of chemical shift databases for protein solid-state NMR: 2D chemical shift maps and amino-acid assignment with secondary-structure information. *J. Biomol. NMR.* **56**, 155–167
68. Li, Q., Babinchak, W. M., and Surewicz, W. K. (2021) Cryo-EM structure of amyloid fibrils formed by the entire low complexity domain of TDP-43. *Nat. Commun.* **12**, 1–8
69. Hu, R., Zhang, M., Chen, H., Jiang, B., and Zheng, J. (2015) Cross-seeding interaction between β-amyloid and human islet amyloid polypeptide. *ACS Chem. Neurosci.* **6**, 1759–1768
70. Zhang, Y., Tang, Y., Zhang, D., Liu, Y., He, J., Chang, Y., *et al.* (2021) Amyloid cross-seeding between Aβ and hIAPP in relation to the pathogenesis of Alzheimer and type 2 diabetes. *Chin. J. Chem. Eng.* **30**, 225–235
71. Zhang, M., Hu, R., Chen, H., Chang, Y., Ma, J., Liang, G., *et al.* (2015) Polymorphic cross-seeding amyloid assemblies of amyloid-β and human islet amyloid polypeptide. *Phys. Chem. Chem. Phys.* **17**, 23245–23256
72. Dasari, A. K., Kayed, R., Wi, S., and Lim, K. H. (2019) Tau interacts with the C-terminal region of α-synuclein, promoting formation of toxic aggregates with distinct molecular conformations. *Biochem* **58**, 2814–2821
73. Lu, J., Zhang, S., Ma, X., Jia, C., Liu, Z., Huang, C., *et al.* (2020) Structural basis of the interplay between α-synuclein and Tau in regulating pathological amyloid aggregation. *J. Biol. Chem.* **295**, 7470–7480
74. Köppen, J., Schulze, A., Machner, L., Wermann, M., Eichentopf, R., Guthardt, M., *et al.* (2020) Amyloid-beta peptides trigger aggregation of alpha-synuclein *in vitro*. *Molecules* **25**, 580–598
75. Candreva, J., Chau, E., Rice, M. E., and Kim, J. R. (2019) Interactions between soluble species of β-amyloid and α-Synuclein promote oligomerization while inhibiting fibrillization. *Biochem* **59**, 425–435

76. Hojjatian, A., Dasari, A. K., Sengupta, U., Taylor, D., Daneshparvar, N., Yeganeh, F. A., *et al.* (2021) Tau induces formation of α-synuclein filaments with distinct molecular conformations. *Biochem. Biophys. Res. Commun.* **554**, 145–150
77. Arseni, D., Hasegawa, M., Murzin, A. G., Kametani, F., Arai, M., Yoshida, M., *et al.* (2022) Structure of pathological TDP-43 filaments from ALS with FTLD. *Nature* **601**, 139–143
78. Fändrich, M., Nyström, S., Nilsson, K. P. R., Böckmann, A., LeVine, H., III, and Hammarström, P. (2018) Amyloid fibril polymorphism: A challenge for molecular imaging and therapy. *J. Intern. Med.* **283**, 218–237
79. Mompeán, M., Li, W., Li, J., Laage, S., Siemer, A. B., Bozkurt, G., *et al.* (2018) The structure of the necrosome RIPK1-RIPK3 core, a human hetero-amyloid signaling complex. *Cell* **173**, 1244–1253
80. Xiao, X., Wang, Y., Seroski, D. T., Wong, K. M., Liu, R., Paravastu, A. K., *et al.* (2021) De novo design of peptides that coassemble into β sheet–based nanofibrils. *Sci. Adv.* **7**, eabf7668
81. Wong, K. M., Shao, Q., Wang, Y., Seroski, D. T., Liu, R., Lint, A. H., *et al.* (2021) CATCH peptides coassemble into structurally heterogeneous β-sheet nanofibers with little preference to β-strand alignment. *J. Phys. Chem. B.* **125**, 4004–4015
82. Wong, K. M., Robang, A. S., Lint, A. H., Wang, Y., Dong, X., Xiao, X., *et al.* (2021) Engineering β-Sheet peptide coassemblies for biomaterial applications. *J. Phys. Chem. B* **125**, 13599–13609
83. Sidhu, A., Segers-Nolten, I., and Subramaniam, V. (2016) Conformational compatibility is essential for heterologous aggregation of α-synuclein. *ACS Chem. Neurosci.* **7**, 719–727
84. Ma, B., and Nussinov, R. (2012) Selective molecular recognition in amyloid growth and transmission and cross-species barriers. *J. Mol. Biol.* **421**, 172–184
85. Chien, P., DePace, A. H., Collins, S. R., and Weissman, J. S. (2003) Generation of prion transmission barriers by mutational control of amyloid conformations. *Nature* **424**, 948–951
86. Huang, D., Hudson, B. C., Gao, Y., Roberts, E. K., and Paravastu, A. K. (2018) Solid-state NMR structural characterization of self-assembled peptides with selective 13 C and 15 N isotopic labels. *Pept. Self-Assembly* **1777**, 23–68
87. Ramamoorthy, A. (2005) *NMR Spectroscopy of Biological Solids*, CRC Press, Boca Raton, FL
88. Puangmalai, N., Bhatt, N., Montalbano, M., Sengupta, U., Gaikwad, S., Ventura, F., *et al.* (2020) Internalization mechanisms of brain-derived tau oligomers from patients with Alzheimer's disease, progressive supranuclear palsy and dementia with Lewy bodies. *Cell Death Dis* **11**, 1–16
89. Cascio, F. L., Garcia, S., Montalbano, M., Puangmalai, N., McAllen, S., Pace, A., *et al.* (2020) Modulating disease-relevant tau oligomeric strains by small molecules. *J. Biol. Chem.* **295**, 14807–14825
90. Puangmalai, N., Sengupta, U., Bhatt, N., Gaikwad, S., Montalbano, M., Bhuyan, A., *et al.* (2022) Lysine 63-linked ubiquitination of tau oligomers contributes to the pathogenesis of Alzheimer's disease. *J. Biol. Chem.* **298**, 10766–10784
91. Fogarty, M. J., Hammond, L. A., Kanjhan, R., Bellingham, M. C., and Noakes, P. G. (2013) A method for the three-dimensional reconstruction of Neurobiotin™-filled neurons and the location of their synaptic inputs. *Front. Neural Circuits.* **7**, 153–161
92. Schätzle, P., Wuttke, R., Ziegler, U., and Sonderegger, P. (2012) Automated quantification of synapses by fluorescence microscopy. *J. Neurosci. Methods* **204**, 144–149
93. Ausdenmoore, B. D., Markwell, Z. A., and Ladle, D. R. (2011) Localization of presynaptic inputs on dendrites of individually labeled neurons in three dimensional space using a center distance algorithm. *J. Neurosci. Methods* **200**, 129–143
94. Tamás, G., Buhl, E. H., Lörincz, A., and Somogyi, P. (2000) Proximally targeted GABAergic synapses and gap junctions synchronize cortical interneurons. *Nat. Neurosci.* **3**, 366–371